Article

Millimeter-Wave Channel Measurements and Path Loss Characterization in a Typical Indoor Office Environment

Lorenzo Rubio [1,*] **, Vicent M. Rodrigo Peñarrocha** [1] **, Marta Cabedo-Fabres** [1] **, Bernardo Bernardo-Clemente** [1] **, Juan Reig** [1] **, Herman Fernández** [2] **, Jesús R. Pérez** [3] **, Rafael P. Torres** [3] **, Luis Valle** [3] **and Óscar Fernández** [3]

1 iTEAM Research Institute, Universitat Politècnica de València, 46022 Valencia, Spain
2 Escuela de Ingeniería Electrónica, Universidad Pedagógica y Tecnológica de Colombia, Sogamoso 152211, Colombia
3 Departamento de Ingeniería de Comunicaciones, Universidad de Cantabria, 39005 Santander, Spain
* Correspondence: lrubio@dcom.upv.es

Abstract: In this paper, a path loss characterization at millimeter-wave (mmWave) frequencies is performed in a typical indoor office environment. Path loss results were derived from propagation channel measurements collected in the 25–40 GHz frequency band, in both line-of-sight (LOS) and obstructed-LOS (OLOS) propagation conditions. The channel measurements were performed using a frequency-domain channel sounder, which integrates an amplified radio over fiber (RoF) link to avoid the high losses at mmWave. The path loss was analyzed in the 26 GHz, 28 GHz, 33 GHz and 38 GHz frequency bands through the *close-in free space reference distance* (CI) and the *floating-intercept* (FI) models. These models take into account the distance dependence of the path loss for a single frequency. Nevertheless, to jointly study the distance and frequency dependence of the path loss, multi-frequency models were considered. The parameters of the ABG (A-alpha, B-beta and G-gamma) and the *close-in free space reference distance with frequency path loss exponent* (CIF) models were derived from the channel measurements in the whole 25–40 GHz band under the minimum mean square error (MMSE) approach. The results show that, in general, there is some relationship between the model parameters and the frequency. Path loss exponent (PLE) values smaller than the theoretical free space propagation were obtained, showing that there are a waveguide effect and a constructive interference of multipath components (MPCs). Since the measurements were obtained in the same environment and with the same configuration and measurement setup, it is possible to establish realistic comparisons between the model parameters and the propagation behavior at the different frequencies considered. The results provided here allow us to have a better knowledge of the propagation at mmWave frequencies and may be of interest to other researchers in the simulation and performance evaluation of future wireless communication systems in indoor hotspot environments.

Keywords: 5G; 6G; channel measurements; indoor communications; indoor hotspot; millimeter-wave; mmWave; path loss models; propagation; wireless channels

1. Introduction

The main objectives of the future wireless communications systems are to provide a high-capacity and high-data rate to offer ultra-reliable and low-latency communications [1–4], but also communications in scenarios with high user density, such as indoor hotspots [5]. The initial deployments of the fifth-generation (5G) of wireless networks are carried out in the sub-6 GHz band. At the European level, the harmonized frequency bands delivered by the second digital dividend (frequencies below 1 GHz) and the 3.5 GHz frequency band are being used [6]. Nevertheless, to meet the 5G systems and beyond, referred to as sixth-generation (6G) systems, large bandwidths are necessary [2,5]. Thus, 5G NR (New Radio) has increased the bandwidth of 20 MHz defined in LTE up to 100 MHz in the sub-6 GHz band (known as Frequency Range 1) and up to 400 MHz in the millimeter-wave

(mmWave) band (known as Frequency Range 2) [7]. The MmWave spectrum offers a great opportunity to increase both capacity and data rate, due to the fact that the bandwidths may be larger than those available in the sub-6 GHz band. Different bands in the mmWave spectrum were identified in the last World Radio Conference (WRC), held in Egypt in 2019 [8]. These bands cover mainly the spectrum ranging from 24.25 GHz to 47 GHz, the 26 GHz, 28 GHz and 38 GHz being the preferred frequency bands for the deployment of future networks. Thus, the 24.25–27.5 GHz band has been recommended by the Radio Spectrum Policy Group for 5G deployments at mmWave frequencies in Europe and in the USA the 27.5–28.35 GHz frequency band was licensed for mobile networks.

The knowledge of the propagation channel plays an important role in the wireless system design, simulation and modeling. In the last few years, many resources and efforts have been dedicated to characterizing propagation channels and numerous research studies related to channel measurements at mmWave frequencies have been published in the literature [9–14]. Channel measurements have been carried out in some voguish frequency bands, such as 15 GHz, 28 GHz, 38 GHz, 45 GHz, 60 GHz and 73 GHz. However, most of these channel measurements have been performed in different environments and under different setup configurations (e.g., time- and frequency-domain channel sounding techniques, bandwidths and antennas), which can impact on the propagation channel characteristics making it difficult to compare the measurement results.

In this work, we present experimental path loss results derived from channel measurements covering the whole 25–40 GHz band. The channel measurements were collected using a frequency-domain channel sounder in an indoor office environment under both line-of-sight (LOS) and obstructed-LOS (OLOS) conditions. In order to reduce the cable losses, which are high at mmWave frequencies, as a novelty an amplified broadband radio over fiber (RoF) link was integrated in the channel sounder. The RoF link increases the dynamic range in the measurement, allowing the use of omnidirectional antennas in both the transmitter (Tx) and receiver (Rx) sides.

The path loss results were particularized in the 26 GHz, 28 GHz, 33 GHz and 38 GHz frequencies bands, where the parameters of single frequency large-scale path loss models were derived from the channel measurements. In this way, since the measurements were obtained in the same environment, and with the same configuration and measurement setup, we can establish realistic comparisons between the models and the frequency bands considered. Taking advantage of the large measured bandwidth (15 GHz, from 25 GHz to 40 GHz), multi-frequency path loss models were also analyzed. The results reported in this study allow us to have a better knowledge of the propagation channel characteristics in this particular environment and in the potential bands to deploy future wireless networks at mmWave frequencies.

This contribution is organized as follows. The propagation environment, measurement setup, methodology and procedure are described in Section 2. Section 3 introduces the large-scale path loss models used in the study, distinguishing between single frequency and multi-frequency path loss models. The results are presented and discussed in Section 4. Finally, Section 5 draws the main conclusions.

2. Propagation Channel Measurements

2.1. Measurement Environment

The channel measurements were performed in a typical indoor office environment of the iTEAM Research Institute facilities at the Universitat Politècnica de València, Spain. This is a modern building, where ceilings and floors are built of reinforced concrete over steel plates, with walls made of wood and plasterboard-paneled. The dimensions of the office are 9.68 m long by 6.93 m wide with a height of 2.63 m. Figure 1 shows a view of the office environment. There are numerous elements that cause diffraction, reflection, scattering and blocking processes at mmWave frequencies, such as chairs, desks with computer screens and steel storage cabinets, among others.

Figure 1. View of the propagation environment where the channel measurements were collected.

2.2. Measurement Setup and Procedure

A channel sounder implemented in the frequency domain by the Keysight N5227A vector network analyzer (VNA) was used to measure the complex channel transfer function (CTF). This channel sounder, with some variants, and the measurement methodology have been used extensively by some of the authors in narrowband and wideband channel measurements performed at microwave and mmWave frequencies. In this work, ultra-wideband omnidirectional antennas (the QPAR QOM-SL-0.8-40-K-SG-L model), with linear (vertical) polarization, were used at the Tx and Rx positions. Figure 2 depicts the radiation pattern of the Tx antenna measured at 26 GHz, 28 GHz, 33 GHz and 38 GHz in our anechoic chamber. As can be observed, the shape of the radiation pattern shows slight changes in the frequency range measured. The measured gain (square marker) of the Tx and Rx antennas in the horizontal plane and the cubic spline interpolation are depicted in Figure 3. The half power beamwidth (HPBW) of the antennas in the elevation plane is about 35° in the frequency range from 25 GHz to 40 GHz. This value of the HPBW is relevant in order to guarantee to collect the maximum number of multipath contributions (MPCs) in propagation channel measurements.
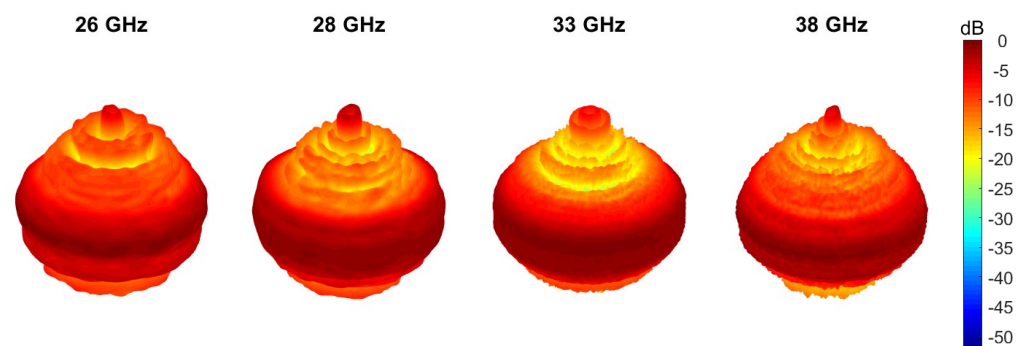

Figure 2. Radiation pattern of the Tx antenna measured at 26 GHz, 28 GHz, 33 GHz and 38 GHz.

An amplified broadband RoF link (the Emcore Optica OTS-2 model), with a gain of 35 dB, was integrated in the channel sounder to connect the antenna to the output port of the VNA (Port 1). The RoF improves the dynamic range of the measurement, reducing the cable losses, and allows the use of omnidirectional antennas, in both the Tx and Rx sides, in order to capture all the horizontal MPCs that reach the Rx.

During the measurements, the Rx antenna was mounted on a horizontal positioning system to emulate a 12×12 virtual uniform rectangular array (URA), with an inter-element separation of 3.04 mm (less than $\lambda/2$ at 40 GHz $\approx$ 3.7 mm). This inter-element separation is about $\lambda/4$ at 26 GHz and $2/5\lambda$ at 38 GHz, covering a local area of about $(11/4)^2\lambda^2$ at 26 GHz and $(22/5)^2\lambda^2$ at 38 GHz in order to capture the small-scale fading effects when the Rx antenna is moving over the URA positions (The received signal can suffer spatial selectivity due to the interference of MPCs at the Rx position. If only one position of the Rx antenna is considered (a single measurement), the interference (constructive or destructive) of the MPCs conditions the value of the path loss because the received signal

could experience a deep fade). A personal computer was used to control both the VNA and the positioning system in order to automate the measurement process. The $S_{21}(f)$ scattering parameter, which is equivalent to the CTF [15], denoted by $H(f)$, was measured directly in the 25–40 GHz frequency band, i.e., a channel bandwidth of 15 GHz was considered (the SPAN in the VNA), 32.5 GHz being the central frequency. The signal level at the Tx port (Port 1) of the VNA was −17 dBm. This is the maximum power to not saturate the amplifier of the electro-optical converter at the input of the RoF link. A schematic of the channel sounder is depicted in Figure 4.
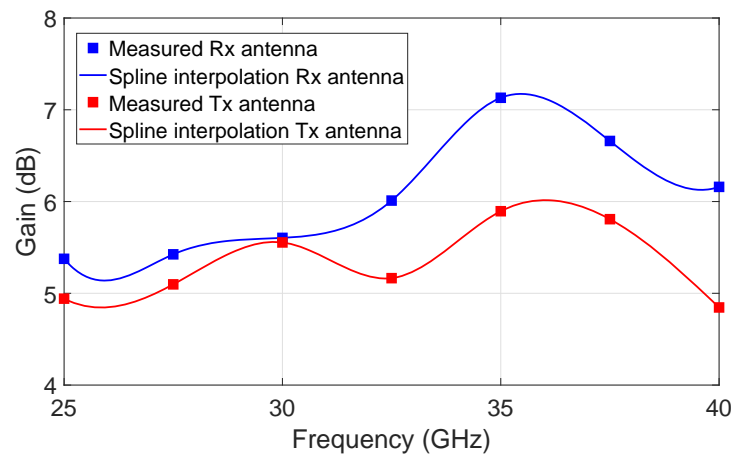

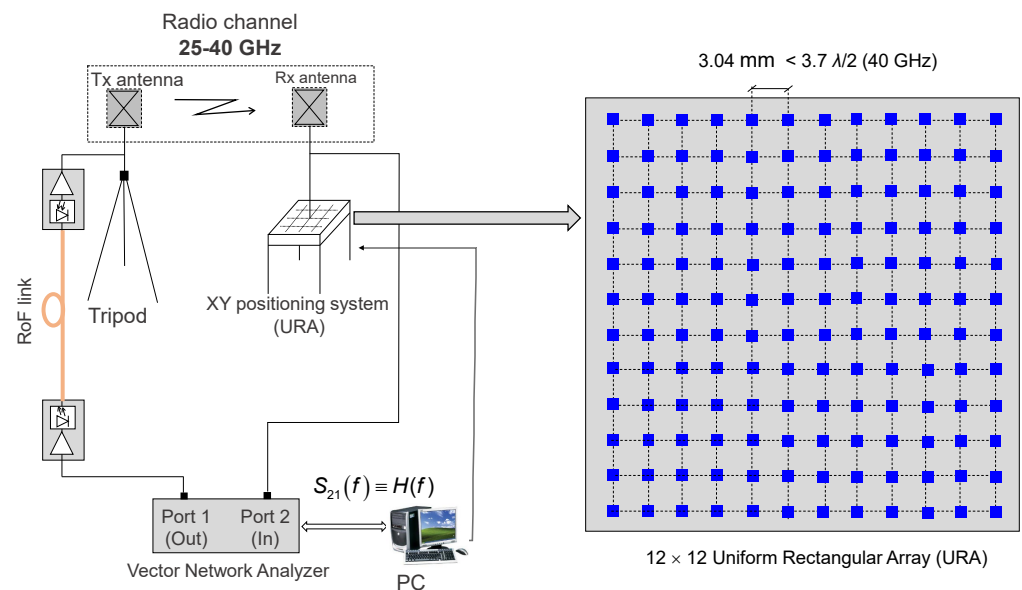**Figure 3.** Measured antennas gain and cubic spline interpolation.

Figure 4. Schematic of the channel sounder used in the propagation channel measurements. The RoF link is placed in the Tx side (Port 1 of the VNA) and the horizontal positioning system in the Rx side (Port 2 of the VNA).

Before doing the channel measurements, a complete response calibration process of the measurement setup is performed to eliminate the losses of cables and connectors, the RoF link response, and phase differences and delays. The response calibration process was performed by disconnecting the Tx and Rx antennas and connecting the transmitter cable output (Tx antenna connector) and receiver cable input (Rx antenna connector) using a female to female K-connector. Due to the fact that the antennas are not included in the calibration process, the measured CTF corresponds to the radio channel, which takes into

account the antennas' response and the propagation channel [16]. For these reasons, it is essential to use wideband antennas in propagation channel measurements.

A total of $N_f = 8192$ frequency points were measured in the 25–40 GHz frequency band (15 GHz of SPAN). Thus, the frequency resolution is $\Delta f \approx 1.83$ MHz (SPAN/N_f). This frequency resolution corresponds to a maximum unambiguous propagation excess delay of $1/\Delta f = 546$ ns, which provides a maximum observable distance of $c_0/\Delta f = 164$ m (with c_0 the speed of light). It is worth noting that this observable distance is larger than the room dimensions, and therefore all the MPCs can be captured.

Another relevant parameter in the measurement process when a VNA is used is the bandwidth of the intermediate frequency (IF) filter. In this work, we have set a bandwidth of 100 Hz. This value is a trade-off between acquisition time (must be low) and dynamic range (a high value is interesting) in the measurement process. Notice that if the bandwidth is low the noise floor decreases, increasing not only the dynamic range (equivalent to the signal-to-noise ratio (SNR) in the measurement) but also the acquisition time. A bandwidth equal to 100 Hz was a common value used by the authors in channel measurements at mmWave frequencies [17]. In other studies published in the literature different values have been considered. For instance, in [11] the authors used a bandwidth equal to 500 Hz in mmWave channel measurements, which is a value higher than the one used in our work. The main parameters and configuration of the channel sounder used in the channel measurements are summarized in Table 1.

Table 1. Channel sounder parameters and configuration used in the channel measurements.

Parameter	Value
VNA output power (Port 1)	−17 dBm
VNA start frequency	25 GHz
VNA end frequency	40 GHz
VNA SPAN (measured bandwidth)	15 GHz
VNA (IF bandwidth)	100 Hz
Frequency points per trace	8192
Tx antenna height	0.90 m
Rx antenna height	1.62 m

The measurements were performed locating the Tx antenna in different positions in order to imitate user equipment (UE) placed on the desk (a laptop, a tablet or a mobile phone, among others). The Rx subsystem (the Rx antenna mounted on the horizontal positioning system) emulates a base station serving the active users in the room, and remained fixed and located close to the wall. From the VNA configuration, the acquisition time to measure the CTF throughout all 144 (12×12) positions of the URA is about 2 h and, in order to guarantee stationary conditions during the measurement process, the measurements were collected at nights, without the presence of people. Due to the channel measurements being carried out for several days, to take into account the temperature changes of the room and the movement of cables when the Tx antenna was displaced, the response calibration was performed every time the Tx antenna was located in a new position just before the measurement. Figure 5 shows the top view of the office room, where the Tx and Rx locations are depicted.

The measurements were obtained in both LOS and OLOS propagation conditions. In LOS, a total of 10 Tx locations (Tx1–Tx10 in Figure 5) were considered, with a Tx–Rx separation distance ranging from 2.70 m to 7.80 m. Figure 6 (left) shows the Rx and the Tx antennas in the Tx1 position. In OLOS, the Tx antenna was located in positions where the direct component was blocked by the computer screens, measured in four Tx locations (Tx11–Tx14 in Figure 5), with a Tx–Rx separation distance from 4.55 m to 8.40 m. Figure 6 (right) shows the Rx and Tx antennas in the Tx14 position. The distance between the Tx and the center of the URA, referred to as the Tx–Rx separation distance, is indicated in

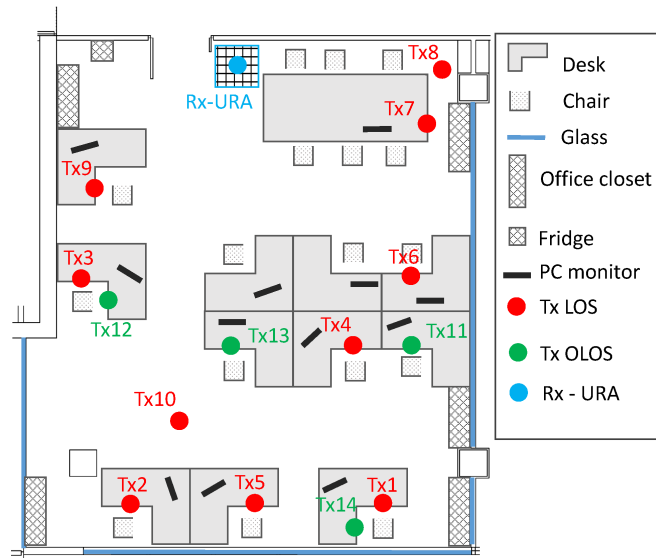Table 2. The height of the Tx and Rx antennas was 0.90 m and 1.62 m above the floor level, respectively.

Figure 5. Top view of the propagation environment.

Figure 6. Tx and Rx antennas in positions Tx1 (**left**) and Tx14 (**right**) in LOS and OLOS, respectively.

Table 2. Distance between the Tx antenna and the center of the URA (in m).

	Tx1	Tx2	Tx3	Tx4	Tx5	Tx6	Tx7	Tx8	Tx9	Tx10	Tx11	Tx12	Tx13	Tx14
Distance	7.80	7.20	4.95	5.10	7.05	4.50	4.05	4.65	2.70	6.00	5.55	4.8	4.55	8.40

2.3. Experimental Path Loss Derivation

The experimental path loss can be derived from the channel measurements averaging the CTF, as indicated in [14,17,18]. Thus, the path loss in logarithmic units (dB), denoted by *PL*, can be obtained as:

$$PL(d) = -10\log_{10}\left(\frac{1}{N_f}\sum_{n=1}^{N_f}\frac{|H(f_n,d)|^2}{g_{Tx}(f_n)g_{Rx}(f_n)M(f_n)}\right), \tag{1}$$

d being the distance between the Tx antenna and the center of the URA, referred to as the Tx–Rx separation distance; f_n the *n*-th frequency sample; and $g_{Tx}(f_n)$ and $g_{Rx}(f_n)$ the Tx and Rx antennas' gain, respectively, in the direction of departure and arrival of the direct MPC (see Appendix A in [14]). The term $M(f_n)$ in (1) considers the antenna mismatch.

If $S_{11}^{\text{Tx}}(f_n)$ and $S_{11}^{\text{Rx}}(f_n)$ are the $S_{11}(f)$ scattering parameters of the Tx and Rx antennas, respectively, $M(f_n)$ can be calculated by the following expression:

$$M(f_n) = (1 - |S_{11}^{\text{Tx}}(f_n)|^2)(1 - |S_{11}^{\text{Rx}}(f_n)|^2). \tag{2}$$

It should be noted that the return loss in ultra-wideband antennas can adopt values higher than -10 dB (a value used as a reference) in some frequencies, it being necessary to introduce the term $M(f_n)$ in (1) in order not to overestimate the path loss of the propagation channel [14].

3. Large-Scale Path Loss Models

There are different approaches to building large-scale path loss models [15,19–21], e.g., the empirical, stochastic and deterministic approaches. Nevertheless, path loss models based on channel measurements provide a more realistic insight into propagation features, in particular in mmWave frequency bands, where describing the propagation environment with a good resolution in terms of the wavelength is difficult, especially when there are many objects interacting with the wavefronts. In this sense, single frequency and multi-frequency path loss models based on channel measurement data can be defined, and their parameters can be derived, for instance, using the minimum mean square error (MMSE) approach. The large-scale path loss models considered in this work will be introduced in the following subsections, distinguishing between single-frequency and multi-frequency path loss models.

3.1. Single-Frequency Path Loss Models

3.1.1. The CI Model

A common path loss model that relates the path loss, in logarithmic units, to the logarithm of the Tx–Rx distance, $\log_{10} d$, is the *close-in free space reference distance* (CI). The CI model has been used in many works at microwave frequencies and more recently to model the path loss at mmWave frequencies [9,12]. In the CI model, the path loss is given by:

$$PL^{\text{CI}}(d) = \text{FSPL}(f, d_0) + 10n \log_{10}(d) + \chi_\sigma^{\text{CI}}, \text{for } d \geq d_0, \tag{3}$$

the term $\text{FSPL}(f, d_0) = 10 \log_{10}(4\pi f d_0 / c_0)^2$ being the free space path loss propagation for a reference Tx–Rx distance equal to d_0. In (3), n is the well known path loss exponent (PLE), which is related to both the propagation conditions and the environment. The large-scale fluctuations of the path loss over distance are modeled by the term χ_σ^{CI}, in logarithmic units, which is a Gaussian random variable with zero mean and standard deviation σ. The term χ_σ^{CI} is also known in the literature as the shadow factor (SF) and it is also an indicator of the goodness of fit of the model.

Path loss models developed in ultra-high frequency (UHF) and microwave bands for macrocellular environments consider a close-in reference distance of 100 m or 1 km. Nevertheless, in indoor environments it is common to use a reference distance equal to 1 m as a standard [9]. Standardizing a reference distance allows comparison of channel measurements made in different environments. In this way, (3) can be rewritten as:

$$PL^{\text{CI}}(d) = \text{FSPL}(f, 1 \text{ m}) + 10n \log_{10}(d) + \chi_\sigma^{\text{CI}}, \text{for } d \geq 1 \text{ m}. \tag{4}$$

Note that the term $\text{FSPL}(f, 1 \text{ m})$ has an inherent frequency dependence of the path loss embedded for a distance equal to 1 m and then the PLE characterizes the dependence of the path loss on the distance.

3.1.2. The FI Model

The *floating-intercept* (FI) path loss model has also been extensively used to characterize the path loss at microwave frequencies, in particular in the sub-6 GHz band, in different

propagation scenarios and wireless applications, e.g., fix-to-mobile and vehicle-to-vehicle communications [9,15,17,22]. In the FI model, the path loss is given by:

$$PL^{\text{FI}}(d) = \beta + 10\alpha \log_{10}(d) + \chi_\sigma^{\text{FI}}, \tag{5}$$

β being an *offset* term, known as the floating-intercept parameter; α the PLE, also related to both propagation conditions and the environment; and χ_σ^{FI} is the SF. In opposition to the CI model, the FI model is based on a curve fitting approach without any physical anchor. In this sense, the FI model exhibits one more degree of freedom than the CI model since it considers two parameters, β and α. The FI model was adopted in channel model standardizations, as for instance in the WINNERII Project and 3GPP propagation models [19,20], and has recently been used at mmWave frequencies [9,17]. Note that the *offset* term does not represent the path loss at any reference distance and the validity of the model parameters are restricted to the distances for which the measured data were carried out.

3.2. Multi-Frequency Path Loss Models

The path loss does not only depend on the distance but also on the frequency. To describe the path loss variations in both distance and frequency, propagation models have emerged as an extension of the single-frequency models.

3.2.1. The ABG Model

The ABG (A-alpha, B-beta and G-gamma) path loss model considers frequency-dependent and distance-dependent terms to describe the large-scale path loss as a function of the frequency as well as the distance [9,23]. In the ABG model, the path loss is given by:

$$PL^{\text{ABG}}(f,d) = 10\alpha \log_{10}\left(\frac{d}{1\,\text{m}}\right) + \beta + 10\gamma \log_{10}\left(\frac{f}{1\,\text{GHz}}\right) + \chi_\sigma^{\text{ABG}}, \tag{6}$$

where $d \geq 1$ m and $f \geq 1$ GHz. The parameters α and γ describe the distance and frequency dependence, respectively; β is the *offset* parameter; f is the frequency expressed in GHz; and χ_σ^{ABG} is the SF term, which describes the mean fluctuations over both distance and frequency. Note that the ABG model is an extension of the FI model for multiple frequencies, thus, setting $\gamma = 0$, Equation (6) becomes (5).

3.2.2. The CIF Model

From the CI model, a simple multi-frequency model is the *close-in free space reference distance with frequency dependent path loss exponent* (CIF), introduced in [9]. In the CIF model, the path loss is given by:

$$PL^{\text{CIF}}(f,d) = \text{FSPL}(f, 1\,\text{m}) + 10n\left(1 + b\left(\frac{f - f_0}{f_0}\right)\right)\log_{10}(d) + \chi_\sigma^{\text{CIF}}, \tag{7}$$

where $d \geq 1$ m and $f \geq 1$ GHz. The parameter n refers to the distance dependency of the path loss, equivalent to the PLE in the CI model. The parameter b represents the slope of linear frequency dependency of the path loss and f_0 is a frequency of reference estimated as:

$$f_0 = \frac{\sum_{k=1}^{K} f_k N_k}{\sum_{k=1}^{K} N_k}, \tag{8}$$

K being the number of frequency samples considered and N_k the number of path loss data points for the k-th frequency. In our work, from the channel measurements configuration, the value of f_0 is 32.5 GHz (the central frequency of the SPAN). In (7), the term χ_σ^{CIF} is the SF. Note that the CIF model becomes the CI model when $b = 0$, or when f_0 is equal to f in the single frequency case.

4. Results

This section presents and discusses the parameters of the path loss models introduced in the previous section.

4.1. Single-Frequency Path Loss Models

For each frequency band analyzed, i.e., 26 GHz, 28 GHz, 33 GHz and 38 GHz, the path loss was derived from the channel measurements over a bandwidth of 2 GHz. Taking into account the frequency resolution, Δf, the number of frequency samples in the path loss derivation was

$$N_f = \lfloor 2\,\text{GHz}/\Delta f - 1 \rfloor = 1091, \tag{9}$$

and (1) is rewritten as:

$$PL(d) = -10 \log_{10}\left(\frac{1}{1091} \sum_{n=1}^{1091} \frac{|H(f_n, d)|^2}{g_{\text{Tx}}(f_n) g_{\text{Rx}}(f_n) M(f_n)} \right). \tag{10}$$

Selecting an odd number of frequency samples, the central frequency sample, f_{546}, corresponds to the frequency band. As an example, the measured path loss (cross marker) at 28 GHz is shown in Figure 7. It can be seen that the measured path loss exhibits a reduced dispersion through all positions of the URA, being less in LOS than in OLOS conditions. Mean values of the path loss (square marker) derived by averaging the measured path loss in all positions of the URA are also depicted in this figure. The path loss fitting results for the CI and the FI models are also shown in Figure 7. The results show that both models produce a good fit to the measured path loss and predict similar values. From Figure 7 the path loss difference between LOS and OLOS conditions is about 5 dB.
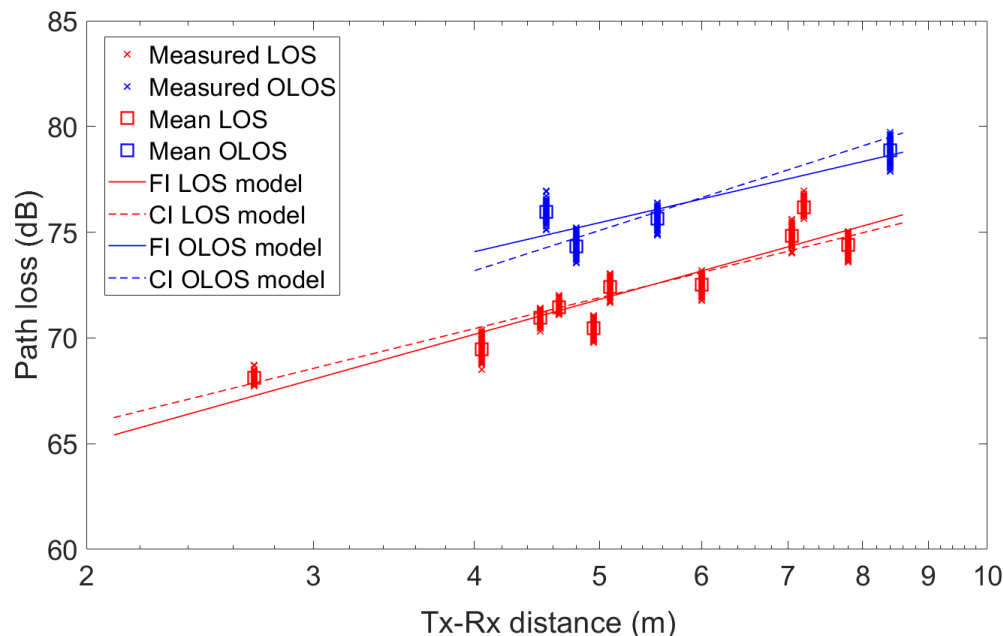

Figure 7. Measured path loss, mean path loss and predicted path loss using the CI and FI models at 28 GHz.

The parameters of the CI and FI models are summarized in Tables 3 and 4, respectively. These parameters, and their 95% confidence intervals, were estimated from the measured data under the MMSE approach using the `cftool` function of Matlab. The standard deviation of the SF term, σ, is also summarized in the tables. For the CI model and LOS conditions, the mean PLE exponent ranges from 1.269 to 1.749, with values lower than free space propagation (PLE of 2). For OLOS conditions, the PLE increases to mean values

close to free space propagation, except at 26 GHz where the mean PLE is 1.785. It is worth noting that values lower than 2 can be explained due to the wideband transmission nature and that in indoor mmWave propagation channel the MPCs can experience constructive interference and a waveguide effect [9,17]. Thus, in [12] values of the PLE equal to 1.45 and 2.18 were measured at 28 GHz for LOS and OLOS conditions, respectively. In [9], lower values were found, where PLE values equal to 1.1 and 1.3 were measured at 28 GHz and 73 GHz in LOS conditions, respectively, using omnidirectional antennas with vertical polarization. Note that the PLE found at 73 GHz is very low compared to the one obtained in our work at the maximum frequency, i.e., a PLE of 1.749 at 38 GHz. These differences are due, in part, to the different characteristics of the propagation environment, so that the PLE exhibits a higher dependence on frequency in this environment.

Table 3. Parameters of the CI model.

Scenario	Frequency	FSPL (f, 1 m)	n ($n_{95\%}$)	σ (dB)
LOS	26 GHz	60.74 dB	1.269 (1.256–1.281)	1.75
	28 GHz	61.38 dB	1.505 (1.498–1.511)	0.93
	33 GHz	62.81 dB	1.733 (1.725–1.740)	1.07
	38 GHz	64.04 dB	1.749 (1.741–1.757)	1.15
OLOS	26 GHz	60.74 dB	1.785 (1.775–1.795)	0.93
	28 GHz	61.38 dB	1.960 (1.950–1.971)	1.00
	33 GHz	62.81 dB	2.203 (2.195–2.212)	0.76
	38 GHz	64.04 dB	2.075 (2.489–2.522)	1.08

Table 4. Parameters of the FI model.

Scenario	Frequency	β ($\beta_{95\%}$) (dB)	α ($\alpha_{95\%}$)	σ (dB)
LOS	26 GHz	59.29 (58.80–59.79)	1.464 (1.396–1.533)	1.73
	28 GHz	59.93 (59.67–60.19)	1.701 (1.665–1.736)	0.90
	33 GHz	60.25 (60.37–60.94)	2.025 (1.986–2.065)	0.99
	38 GHz	61.49 (61.19–61.80)	2.094 (2.052–2.136)	1.06
OLOS	26 GHz	60.01 (59.46–60.16)	1.880 (1.808–1.952)	0.92
	28 GHz	65.56 (65.07–66.05)	1.415 (1.351–1.480)	0.82
	33 GHz	67.18 (66.89–67.46)	1.634 (1.597–1.671)	0.47
	38 GHz	71.24 (70.97–71.51)	1.135 (1.100–1.171)	0.45

From Table 4, the PLE derived in the FI model, the α parameter, is higher than the PLE in the CI model in LOS, whereas in OLOS the values are significantly lower, except at 26 GHz. In LOS conditions the mean value of α increases with the frequency, ranging from 1.464 to 2.094, close to the free space propagation at 33 and 38 GHz. Furthermore, the *offset* term, the β parameter, increases with the frequency, with values ranging from 59.29 dB to 61.49 dB. Nevertheless, in OLOS conditions the parameters α and β experience different behavior, where the mean value of α is smaller in comparison to the LOS condition, and also shows a decreasing trend with the frequency, from 1.880 to 1.135 at 26 GHz and 38 GHz, respectively. The decrease in the mean value of α is accompanied by an important increase in the *offset* term, thus β adopts larger values in comparison to LOS conditions, resulting in higher path loss in OLOS, as expected (When the FI model is considered, there may be propagation conditions where a reduction of the PLE is accompanied by an increase in the *offset* term, resulting in higher losses as the distance, or frequency, increases. This behavior was observed by the authors in V2V channel measurements, where an inverse relationship between the PLE and the *offset* term was verified (see Figure 10 in [24]). Note that at 38 GHz the mean value of β is 71.24 dB, about 10 dB higher than the value derived for LOS (61.49 dB). The values of the α parameter derived here are higher than the values reported in [9], where values of 1.2 and 0.5 were derived at 28 GHz and 73 GHz, respectively, in LOS

conditions; whereas they are in line with the values published in [12], where a mean value close to 2 was reported at 28 GHz in LOS conditions.

Regarding the standard deviation of the SF term, from Tables 3 and 4 the mean values are very similar in the CI model in both LOS and OLOS propagation conditions, and the values also very close to those obtained in the FI model in LOS conditions. Nevertheless, the values derived in the FI model are lower in OLOS conditions, with a maximum difference of 0.81 dB at 26 GHz and 0.61 dB at 38 GHz. Only in the FI model for OLOS, a decreasing trend with the frequency seems to be intuited, in this case decreasing from 0.92 (at 26 GHz) to 0.45 dB (at 38 GHz). This fact is relevant, because the results suggest that there is no correlation with the frequency in LOS conditions and only certain correlations can appear in OLOS conditions when the FI model is considered. On the other hand, it is worth noting that the shadowing effects are related to the features of the propagation environment, so that high values are related to a highly changing environment and vice versa. The values derived in this work are lower than others published in the literature. For example, in [9] values close to 1.8 dB were obtained at 28 GHz and the difference may be due to the type of environment, which is more homogeneous in our case.

Multi-Frequency Path Loss Models

The variation of the parameters of the single frequency path loss models indicates a clear dependence on the frequency in both LOS and OLOS propagation conditions for the Tx–Rx distances considered. As an example, Figure 8 shows the measured path loss in terms of the frequency for the Tx-4 and Tx-5 positions. The path loss was derived in steps of 0.5 GHz using a bandwidth of 2 GHz. In the figure, the dashed line indicates a trend showing that the path loss increases with the frequency, although there is a frequency selective behavior due to the MPCs' interference at the receiver position and also to the frequency dependence of reflection and diffraction losses. A similar behavior was observed in the other Tx antenna positions. For these reasons, it is appropriate to consider multi-frequency models describing the path loss variations on both distance and frequency.
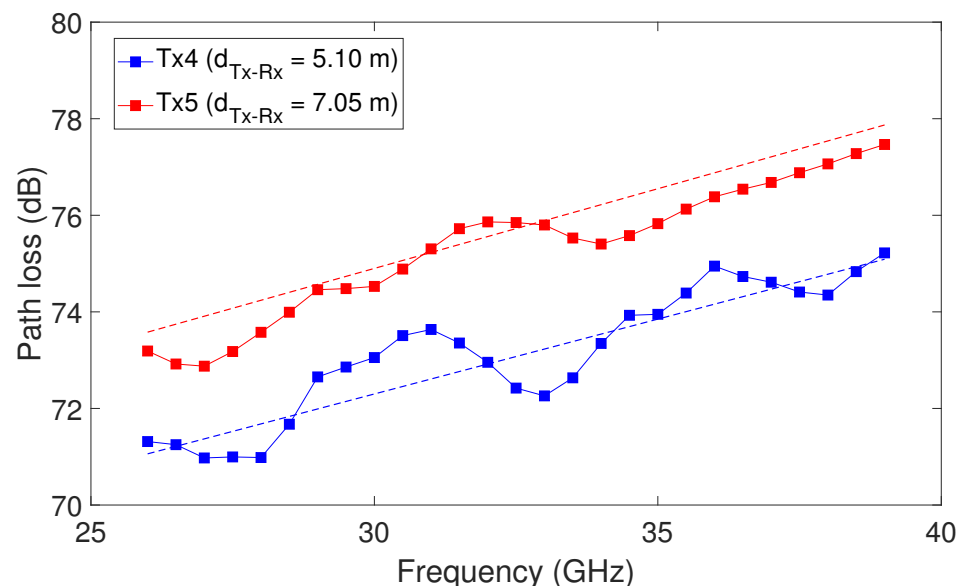

Figure 8. Path loss in terms of the frequency for Tx-4 and Tx-5 positions. The dashed lines indicate a trend obtained from a linear regression fit.

The scatter plot of the measured path loss and the fitting results for the CIF model are shown in Figures 9 and 10 for LOS and OLOS, respectively. The mean values of the CIF model parameters, and the 95% confidence intervals, are summarized in Table 5. These parameters have also been derived using the `cftool` function of Matlab. To take into account the frequency dependence, the measured path loss data considered in the fitting

process are derived for central frequencies ranging from 26 GHz to 39 GHz in steps of 0.5 GHz and for a bandwidth of 2 GHz. The PLE in the multi-frequency CIF model obtained (1.434) is lower than the values derived in the single-frequency CI model (from 1.269 to 1.749) in LOS conditions. Nevertheless, this does not imply that the losses predicted by the CIF model are lower, since the parameter b establishes a dependence of the path loss on the frequency. For OLOS conditions, both the PLE (2.088) and the parameter b (0.302) are significantly higher compare to the LOS conditions, showing a higher dependence of the path loss on the frequency. Regarding the SF standard deviation, the CIF model yields a higher value in both LOS (1.41 dB) and OLOS (1.14 dB), with minor differences in OLOS compared to the CI model, where the SF standard deviation ranges from 0.93 dB to 1.08 dB.
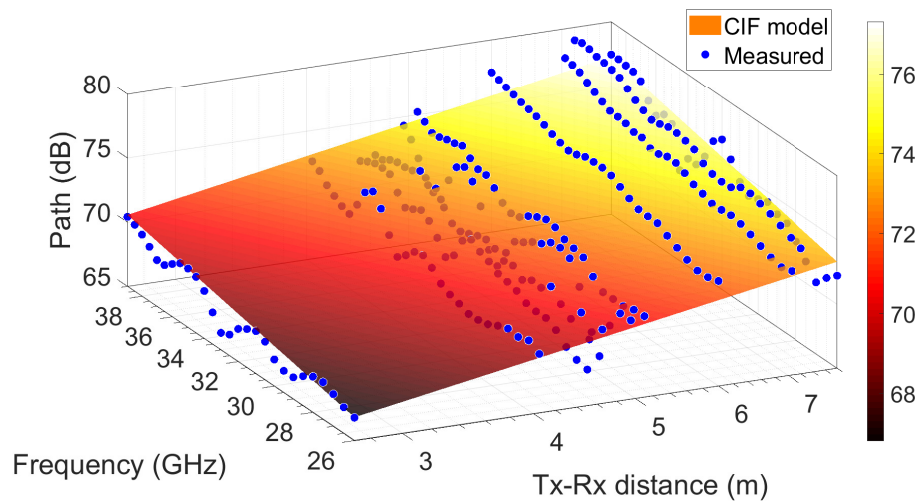
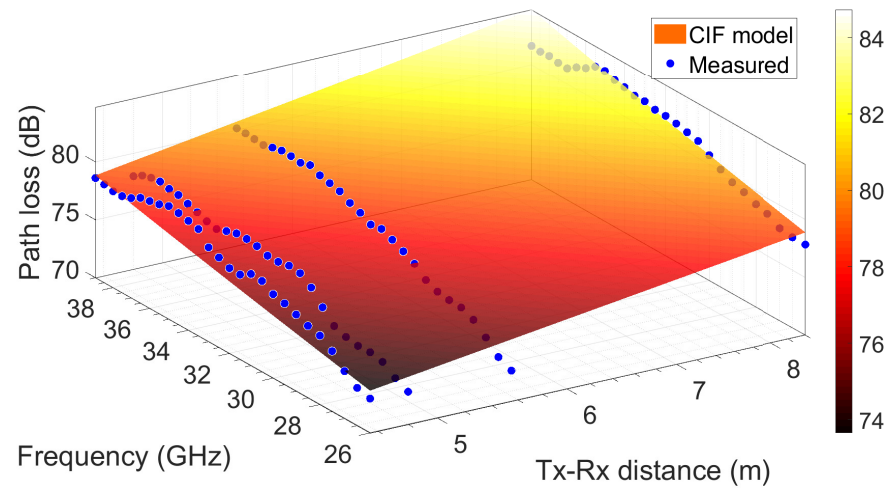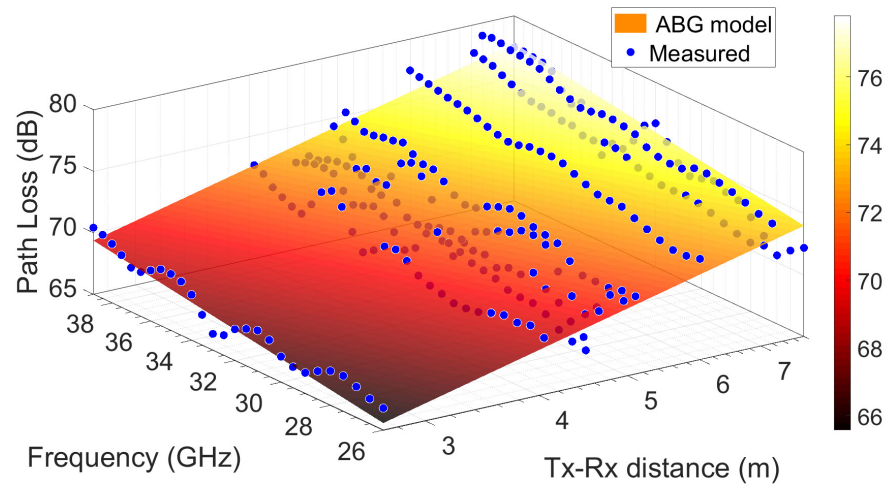**Figure 9.** Measured and CIF path loss model in LOS conditions.

Figure 10. Measured and CIF path loss model in OLOS conditions.

Table 5. Parameters of the multi-frequency CIF model.

Scenario	b ($b_{95\%}$)	n ($n_{95\%}$)	σ (dB)
LOS	0.093 (−0.0427,0.2298)	1.434 (1.411,1.458)	1.41
OLOS	0.302 (0.1776,0.4263)	2.088 (2.057,2.119)	1.14

Figures 11 and 12 show the scatter plot of the measured path loss and the fitting results for the ABG model. The mean values of the model parameters are summarized in Table 6. The PLE, α parameter, is 1.829 and 1.475 in LOS and OLOS conditions, respectively,

and it is in accordance with the single-frequency FI model, where the PLE is also lower in OLOS. The γ parameter, which establishes the dependence on the frequency, is also higher in OLOS, with a mean value of 3.220 compared to the value of 2.153 in LOS. The SF standard deviation adopts higher values (1.32 dB and 1.01 dB in LOS and OLOS conditions, respectively) compared to the mean values derived in the FI model. Comparing the SF standard deviation values in both multiple-frequency models, the ABG model provides slightly lower values (about one tenth of dB); this can be explained because the ABG model introduces one more fitting parameter.

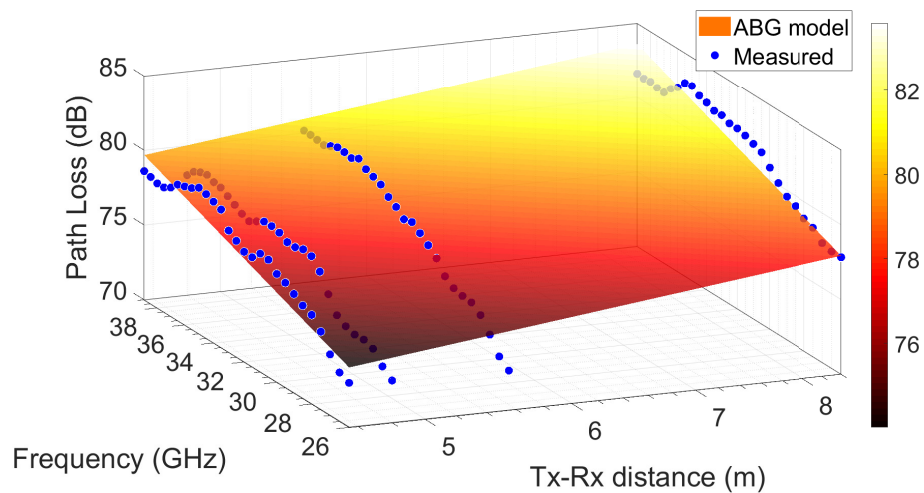**Figure 11.** Measured and ABG path loss model in LOS conditions.

Figure 12. Measured and ABG path loss model in OLOS conditions.

Table 6. Parameters of the multi-frequency ABG model.

Scenario	α ($\alpha_{95\%}$)	β ($\beta_{95\%}$) (dB)	γ ($\gamma_{95\%}$)	σ (dB)
LOS	1.829 (1.709,1.950)	27.22 (22.59,31.84)	2.153 (1.852,2.454)	1.32
OLOS	1.475 (1.289,1.660)	18.74 (13.01,24.48)	3.220 (2.851,3.588)	1.01

In [25], the parameters of the CIF and the ABG models are reported based on channel measurements at 28 GHz and 73 GHz in indoor LOS conditions. For the CIF model the parameters are $n = 1.2$, $b = 0.18$ and a SF standard deviation $\sigma = 2.1$ dB; and for the ABG model the parameters are $\alpha = 0.9$, $\beta = 26.8$ dB, $\gamma = 2.6$ and $\sigma = 1.8$ dB. In [26], for channel measurements at 6.5 GHz, 10.5 GHz, 15 GHz, 19 GHz, 28 GHz and 38 GHz, the

parameters derived using the ABG model are $\alpha = 1.1$, $\beta = 15.7$ dB, $\gamma = 3.1$ and $\sigma = 3.2$ dB. Although the mean values and their 95% confidence intervals are in accordance with those published, it should be noted that there are significant differences. Note that our results are derived in the 25–40 GHz frequency band in steps of 0.5 GHz, while in other works only two frequencies (e.g., 28 GHz and 38 GHz) are considered in the 25–40 GHz frequency band, and in many cases with frequencies very far apart (e.g., 6.5 GHz and 73 GHz), increasing the PLE and, mainly, the SF standard deviation. In this sense, the models and their parameters reported here allow us to describe in good detail the path loss propagation in potential bands to deploy future indoor systems in the 25–40 GHz mmWave frequency band.

5. Conclusions

In this work, a path loss characterization at mmWave frequencies is performed in a typical indoor office environment. The results were derived from propagation channel measurements carried out from 25 GHz to 40 GHz using a frequency-domain channel sounder. An amplified broadband RoF link to avoid the high losses introduced by cables at these frequencies was used, thus increasing the dynamic range in the measurement and allowing the use of omnidirectional antennas. The channel measurements were collected in both LOS and OLOS conditions. Different large-scale path loss models were analyzed based on the measured propagation data, and their parameters were derived under the MMSE approach.

The PLE values derived from the channel measurements are lower, and in some cases smaller, than the theoretical free space propagation PLE ($n = 2$). This is due to constructive interference of MPCs and a waveguide effect that can occur in indoor and confined environments. For the CI model, the PLE ranges from 1.269 (at 26 GHz) to 1.749 (at 38 GHz) in LOS conditions and from 1.785 (at 26 GHz) to 2.203 (at 33 GHz) in OLOS conditions. In both propagation conditions the PLE increases with the frequency, with a higher growth in LOS. The SF standard deviation fluctuates in the interval from 0.76 dB (at 33 GHz in OLOS conditions) to 1.75 dB (at 26 GHz in LOS conditions), not observing any correlation in frequency. For the FI model, the PLE ranges from 1.464 (at 26 GHz) to 2.094 (at 38 GHz) in LOS conditions and from 1.880 (at 26 GHz) to 1.135 (at 38 GHz) in OLOS conditions. In this case, the PLE increases with the frequency in LOS as in the CI model, but the PLE exhibits a reduction with the frequency in OLOS. In this last case, the decrease of the PLE with the frequency is accompanied by an increase in the *offset* term, the β parameter, resulting in higher losses in OLOS, as expected. This behavior was also observed in V2V channel measurements by some of the authors [22,24], where high PLEs correspond to low values of β. The SF standard deviation in the FI model adopts similar values to the CI model in LOS but, on the contrary, it presents lower values in OLOS conditions with a decreasing trend with the frequency, ranging from 0.92 dB (at 26 GHz) to 0.45 dB (at 38 GHz). The similar values of the SF standard deviation indicate that both models exhibit a good fit to the measured path loss and predict similar values.

The multi-frequency models analyzed allow the path loss variations on both distance and frequency to be described. The parameters of the CIF and the ABG models were derived from the channel measurements in the whole 25–40 GHz frequency band, in steps of 0.5 GHz and under a bandwidth of 2 GHz. The PLE derived in the CIF model is 1.434 in LOS conditions and 2.088 in OLOS conditions. These values are in accordance to the values derived in the CI model. For the ABG model the PLE derived is 1.829 in LOS conditions, higher than the PLE in the CIF model, and 1.475 in OLOS conditions. These values are also in accordance with the PLE obtained in the FI model. In both multi-frequency models, the SF standard deviation exhibits a higher value than those obtained in the single-frequency models, being high in LOS conditions (1.41 dB and 1.32 dB in the CIF and ABG models, respectively).

The results provided here allow us to have a better knowledge of the path loss characteristics at mmWave frequencies in indoor office environments, and may assist researchers in simulating and evaluating the performance of future wireless systems in this type of environment.

Abbreviations

The following abbreviations are used in this manuscript:

5G	Fifth-generation
6G	Sixth-generation
ABG	A-alpha, B-beta and G-gamma path loss model
CI	Close-in free space reference distance path loss model
CIF	Close-in free space reference distance with frequency dependent path loss exponent
CTF	Channel transfer function
DUT	Device under test
FI	Floating-intercept path loss model
HPBW	Half power beamwidth
IF	Intermediate frequency
LOS	Line-of-sight
LTE	Long term evolution
mmWave	Millimeter wave
MPC	Multipath contribution
NR	New radio
OLOS	Obstructed-LOS
PLE	Path loss exponent
SNR	Signal-to-noise ratio
RoF	Radio over fiber
SF	Shadow factor
Rx	Receiver
Tx	Transmitter
UE	User equipment
UHF	Ultra-high frequency
URA	Uniform rectangular array
VNA	Vector network analyzer
WRC	World Radiocommunication Conference

References

1. Andrews, J.G.; Buzzi, S.; Choi, W.; Hanly, S.V.; Lozano, A. What will 5G be? *IEEE J. Sel. Areas Commun.* **2014**, *32*, 1065–1082. [CrossRef]
2. Samsung R&D. 5G Vision. 2015. Available online: https://images.samsung.com/is/content/samsung/p5/global/business/networks/insights/white-paper/5g-vision/global-networks-insight-samsung-5g-vision-2.pdf (accessed on 24 October 2022).
3. Tataria, H.; Shafi, M.; Dohler, M.; Sun, S. Six critical Challenges for 6G Wireless Systems: A summary and Some Solutions. *IEEE Veh. Technol. Mag.* **2022**, *17*, 16–26. [CrossRef]
4. Alsharif, M.H.; Kekechi, A.H.; Albreem, M.A.; Chaydhry, S.A.; Zia, M.S.; Kim, S. Sixth Generation 6G wireless networks: Vision, research activities, challenges and potential solutions. *Symmetry* **2020**, *12*, 676. [CrossRef]

5. Giordani, M.; Polese, M.; Mezzavilla, M.; Ragan, S.; Zorzi, M. Toward 6G Networks: Use cases and technologies. *IEEE Commun. Mag.* **2020**, *58*, 55–61. [CrossRef]

6. European Commission—Radio Spectrum Policy Group. Strategic Roadmap towards 5G for Europe. 2016. Available online: https://rspg-spectrum.eu/wp-content/uploads/2013/05/RPSG16-032-Opinion_5G.pdf (accessed on 24 October 2022).

7. 3GPP Technical Report (TR) 21.915. Release 15 Description. 2019. Available online: https://www.etsi.org/deliver/etsi_tr/121900_121999/121915/15.00.00_60/tr_121915v150000p.pdf (accessed on 24 October 2022).

8. Resolution 238. In Proceedings of World Radiocommunication Conference 2019 (WRC-19), Sharm el-Sheikh, Egypt, 28 October–22 November 2019.

9. MacCartney, G.R.; Rappaport, T.S.; Sun, S.; Deng, S. Indoor office wideband millimeter-wave propagation measurements and channel models at 28 GHz and 73 GHz for ultra-dense 5G wireless networks (invited paper). *IEEE Access* **2015**, *3*, 2388–2424. [CrossRef]

10. Haneda, K.; Järveläinen, J.; Karttunen, A.; Kyrö, M.; Putkonen, J. A statistical spatio-temporal radio channel model for large indoor environments at 60 and 70 GHz. *IEEE Trans. Antennas Propag.* **2015**, *63*, 2694–2704. [CrossRef]

11. Huang, J.; Wang, C.X.; Feng, R.; Zhang, W.; Yang, Y. Multifrequency mmWave massive MIMO channel measurements and characterization for 5G wireless communications systems. *IEEE J. Sel. Areas Commun.* **2017**, *35*, 1591–1605. [CrossRef]

12. Tang, P.; Zhang, J.; Shafi, M.; Dmochwski, P.A.; Smith, P.J. Millimeter wave channel measurements and modeling in an indoor hotspot scenario at 28 GHz. In Proceedings of the 2018 IEEE 88th Vehicular Technology Conference (VTC-Fall), Chicago, IL, USA, 27–30 August 2018; pp. 1–5.

13. Rodrigo-Peñarrocha, V.M.; Rubio, L.; Reig, J.; Juan-Llácer, L.; Pascual-García, J.; Molina-Garcia-Pardo, J.M. Millimeter wave channel measurements in an intra-wagon environment. In Proceedings of the COST CA15104 TD(18)07040, Cartagena, Spain, 29 May 2018; pp. 1–5.

14. Rubio, L.; Torres, R.P.; Rodrigo Peñarrocha, V.M.; Pérez, J.R.; Fernández, H.; Molina-García-Pardo, J.-M.; Reig, J. Contribution to the channel path loss and time-dispersion characterizacion in an office environment at 26 GHz. *Electronics* **2019**, *8*, 1261. [CrossRef]

15. Molisch, A.F. *Wireless Communications*, 2nd ed.; Wiley-IEEE Press: Chichester, UK, 2010.

16. Steele, R.; Hanzo, L. *Mobile Radio Communications*, 2nd ed.; Wiley: Chichester, UK, 1999.

17. Rubio, L.; Rodrigo Peñarrocha, V.M.; Molina-García-Pardo, J.-M.; Juan-Llácer, L.; Pascual-García, J.; Reig, J.; Sanchis-borras, C. Millimeter wave channel measurements in an intra-wagon environment. *IEEE Trans. Veh. Technol.* **2019**, *68*, 12427–12431. [CrossRef]

18. Rubio, L.; Reig, J.; Fernández, H.; Rodrigo-Peñarrocha, V.M. Experimental UWB propagation channel path loss and time-dispersion characterization in a laboratory environment. *Int. J. Antennas Propag.* **2013**, *2013*, 35017. [CrossRef]

19. Meinilä, J.; Kyösti, P.; Jämsä, T.; Hentilä, L. *WINNER II Channel Models*; IST-4-027756-WINNER, Tech. Rep. D1.1.2; Inf. Soc. Technol. 2007. Available online: https://www.cept.org/files/8339/winner2%20-%20final%20report.pdf (accessed on 24 September 2019).

20. 3GPP TR 25.996. *Spatial Channel Model for Multiple Input Multiple Output (MIMO) Simulations*; ETSI Technical Repport 125 996; ETSI: Sophia Antipolis, France, 2012.

21. Rappaport, T.S.; MacCartney, G.R.; Samini, M.K.; Sun, S. Wideband millimeter-Wave propagation measurements and channel models for future wireless communication system design. *IEEE Trans. Commun.* **2015**, *63*, 3029–3056. [CrossRef]

22. Fernández, H.; Rubio, L.; Rodrigo Peñarrocha, V.M.; Reig, J. Path loss characterization for vehicular communications at 700 MHz and 5.9 GHz under LOS and NLOS conditions. *IEEE Antennas Wireless Propag. Lett.* **2014**, *13*, 931–934. [CrossRef]

23. Piersanti, S.; Annoni, L.A.; Cassioli, D. Millimeter waves channel measurements and path loss models. In Proceedings of the 2012 IEEE International Conference on Communications, Ottawa, ON, Canada, 10–15 June 2012; pp. 1–5.

24. Fernández, H.; Rubio, L.; Reig, J.; Rodrigo-Peñarrocha, V.M.; Valero, A. Paht loss modeling for vehicular systems performance and communications protocols evaluation. *Mobile Netw. Appl.* **2013**, *18*, 755–765. [CrossRef]

25. Sun, S.; MacCartney, G.R.; Rappaport, T.S. Millimeter-wave distance-dependent large-scale propagation measurements and path loss models for outdoor and indoor 5G systems. In Proceedings of the 2016 10th European Conference on Antennas and Propagation (EuCAP), Davos, Switzerland, 10–15 April 2016; pp. 1–5.

26. Al-Samman, A.M.; Rahman, T.A.; Azmi, M.H.; Hindia, M.N.; Khan, I.; Hanafi, E. Statistical modelling and characterization of experimental mm-Wave indoor channels for future 5G wireless communication networks. *PLoS ONE* **2019**, *11*, e0163034. [CrossRef] [PubMed]